

Utilization of the Wavefront Sensor and Short-Exposure Images for Simultaneous Estimation of Static Speckle and Exoplanet Intensity

Richard A. Frazin¹

rfrazin@umich.edu

ABSTRACT

Heretofore, the literature on exoplanet detection with coronagraphic telescope systems has paid little attention to the information content of short exposures and methods of utilizing the phase measurements of adaptive optics wavefront sensors. This paper provides a framework for incorporation of the wavefront sensor measurements in the context of observing modes in which the science camera takes very short exposures. In this formulation, the wavefront sensor measurements provide a means to jointly estimate the static speckle and the planetary signal. For simplicity, the mathematical development assumes a simple optical system with an idealized Lyot coronagraph. Unlike currently used methods, in which increasing the observation time beyond a certain threshold is useless, this method produces estimates whose error covariances are inversely proportional to the observation time due to the fact that the (quasi-)static speckle and planetary emission are jointly estimated. The method can easily be extended to include angular (due to diurnal field rotation) and spectral diversity.

Numerical experiments are performed with wavefront data from the AEOS Adaptive Optics System sensing at 850 nm. These experiments assume a science camera wavelength of 2.2μ , that the measured wavefronts are exact, an ideal coronagraph, and a Gaussian approximation of shot-noise. A number of static aberrations are introduced, including one with a spatial frequency exactly corresponding to the planet location. Using only 4 seconds of observation time, a planetary intensity of ~ 0.2 photons/millisecond, a stellar intensity of ~ 9 photons/millisecond/pixel at the planet's location, the short-exposure estimation method recovers the correct amplitudes of all static aberrations as well the correct planet brightness with a contrast ratio of 10^{-6} with 17% accuracy. The ideal coronagraph itself provides about 95% extinction in the frames with the highest Strehl ratios.

¹*Dept. of Atmospheric, Oceanic and Space Sciences, University of Michigan, Ann Arbor, MI 48109*

Subject headings: exoplanet detection

1. Introduction and Motivation

The idea of using millisecond exposures for ultra high contrast imaging, such as is required for exoplanet science, has been given little attention due a variety of issues ranging from detector readout noise, to high-volume data management and undeveloped computational methodologies. The method advocated here is to record the intensity in the science camera simultaneously with the wavefront sensor (WFS) measurements, use WFS measurements to estimate the adaptive optics (AO) residual phase and solve a large inverse problem to simultaneously determine the quasi-static (QS) aberrations and the planetary emission. The opinion of this author, which he hopes exoplanet imaging community will gradually begin to adopt, is that the combination of millisecond exposures and the measurements of the WFS provide much more ability to estimate the QS aberrations and the planetary emission than do long-exposure measurements, even when combined with a scheme to estimate QS aberrations, such as a focal plane mask. Intuitively, there are two main reasons for this. The first reason is that the random AO residual phase provides a new pupil plane phase screen every millisecond, which completely de-correlates on the time-scale of the wind blowing across the telescope aperture, the so-called “atmospheric clearing time”, τ_c (McIntosh et al. 2005). Thus, every τ_c seconds AO residual provides a statistically independent phase screen which modulates the quasi-static speckles in a new way. Each new phase screen provides more diversity in the observations and gives more power to estimate the QS aberrations and the spatial distribution of planetary emissions. In contrast, using a focal plane mask and with long-exposure images to estimate errors introduces non-common path errors, and the focal plane mask provides only one measurement with no diversity. However, a focal plane mask could be combined with short-exposure imaging to increase the diversity, using a methodology quite similar to the one advocated here. The second reason for advocating millisecond images is that short-exposure measurements takes advantage of the times when the random temporal modulation greatly reduces the intensity of the speckle background (at a given spatial point). These moments provide much more information about the planetary emission than other times due to the statistical properties of photon noise, particularly the fact that variance of the Poisson distribution is equal to its mean (in other words, there is less shot-noise at instances when the speckle background is faint). This is much more powerful than the so-called “dark speckle” method described by Labeyrie (1995), because the WFS information and estimate of the QS aberrations allow estimation of the relative contributions of the star and planet.

Little work of a similar nature has been published, but Roggemann and Meinhardt (1993) used wave-front sensor measurements to deconvolve images, but did not consider the effects of quasi-static speckle, which are critical for high-contrast imaging. Gladysz et al. (2010) explored short-exposure statistics of on- and off-axis emission, and showed that the resulting histograms provide some means to discriminate between planetary emission and speckle. However, reducing the intensity time-series to histograms discards much information, especially WFS’ estimate of the AO residual phase, which is the function that is driving the temporal modulation in the first place. Fusco and Conan (2004) studied the differences between on- and off-axis intensity statistics of the Strehl ratio in order to define the size of the anisoplanatic region in adaptive optics (AO) images.

The current state-of-the-art methods, always applied to long exposure images, attempt to subtract the point spread function (which includes the effects of QS aberrations) by taking advantage diversity introduced by the diurnal field rotation, multiple spectral channels and/or observations of naked stars with the telescope in a (hopefully) similar state. The most well-known of these are called Angular Differential Imaging (ADI; Marois et al. 2006), and Locally Optimized Combination of Images (LOCI; Lafrenière et al. 2007). At the time of this writing, the latest variant along these lines utilizes principle components analysis to treat some of the difficulties of ADI and LOCI (including overly-aggressive subtraction and bias) and is called Karhunen Loève Image Projection (KLIP) algorithm (Soummer et al. 2012). An independent line of thought in exoplanet detection involving the scanning Hotelling Observer has been proposed by Caucci et al. (2007, 2009), who did not consider the effects of QS aberrations or a coronagraph (cf. Sec. 3 below). The work here is most related to that of Sauvage et al. (2010), in which the authors proposed to use an analytical coronagraph model to simultaneously estimate the planetary emission and the stellar background from a long-exposure image. The most significant difference between this work and that of Sauvage et al. (2010) is the incorporation of WFS data and short-exposure images. It is shown here that the incorporation of short-exposure images has much more potential to estimate weak planetary signals than long exposure images.

2. A Simple Coronagraph Model

As the aim of the present work is to illustrate the potential of combining the WFS signal with short-exposure images in the science camera, the model is idealized, following Sauvage et al. (2010). Consider a telescope with an AO system feeding a stellar coronagraph, shown schematically in Fig. (1). Shown here is stellar variant of the classic Lyot coronagraph (Lyot 1939), versions of which have been used to study the Sun’s corona for many decades.

In a Lyot coronagraph, light is first focused onto a focal-plane occulter, onto which the image of the star falls. The light that misses the occulter is then re-collimated and passed through the so-called Lyot stop, which removes much of the star light diffracted by the focal plane mask.

Assume an aperture function $A(\mathbf{r})$, where \mathbf{r} is the 2D spatial coordinate in the pupil plane. In this formulation, $A(\mathbf{r})$ is assumed to include the effect of the Lyot stop in the coronagraph system (Sauvage et al. 2010). Above the atmosphere, the field due to the on-axis star is given simply by the constant u_* , and the field due to the planet is given by the linear phase-angle function $u_\bullet \exp[jk\boldsymbol{\alpha}_p \cdot \mathbf{r}]$, where u_\bullet/u_* is the square-root of intensity contrast ratio between the star and the planet, $k = 2\pi/\lambda$ and λ is the wavelength at the central wavelength of observation, and $\boldsymbol{\alpha}_p$ is the 2D direction vector ($\|\boldsymbol{\alpha}_p\| < 1$) indicating the location of the planet. This is easily generalized to multiple planets and extended objects (e.g., protoplanetary disks) with superposition of sources at angles $\{\boldsymbol{\alpha}_k\}$. We take the AO residual phase to be given by $\phi_r(\mathbf{r}, t)$ and the upstream (of the coronagraph) static aberrations (leading to so called quasi-static speckle) are given by $\phi_u(\mathbf{r})$, for a total wavefront phase aberration given by:

$$\phi(\mathbf{r}, t) \equiv \phi_r(\mathbf{r}, t) + \phi_u(\mathbf{r}). \quad (1)$$

Generally speaking one expects that $\|\phi_u(\mathbf{r})\| \ll \|\phi_r(\mathbf{r}, t)\|$. The importance of ϕ_u is due to the fact that it changes on very long time scales compared to ϕ_r and hence creates speckles that cannot be mitigated by long integrations. For simplicity, static aberrations downstream of the coronagraph, which are generally considered to be less important than upstream aberrations, are not considered, see Sauvage et al. (2010) for a discussion. The analysis here permits amplitude effects by allowing ϕ_r and ϕ_u to be complex valued functions. We assume that the planet and the star are in close enough proximity so that they are in the same isoplanatic patch, but are separated enough for the planet to be beyond the influence of the coronagraph, i.e., $\theta_{\text{in}} < \|\boldsymbol{\alpha}_p\| < \theta_{\text{iso}}$, where θ_{in} is the inner-working-angle of the coronagraph and θ_{iso} is the isoplanatic angle.

Without loss of generality, we assume that the spatial average AO residual phase over the pupil is zero:

$$\phi_{r0}(t) \equiv \int d^2\mathbf{r} A(\mathbf{r}) \phi_r(\mathbf{r}, t) = 0, \quad (2)$$

as the value of ϕ_{r0} does not have any effect on the intensity. Thus, the pre-coronagraph pupil plane fields of the star and planet are given by:

$$u_s^-(\mathbf{r}, t) = u_* A(\mathbf{r}) \exp[j\phi(\mathbf{r}, t)] \quad (3)$$

$$u_p(\mathbf{r}, t) = u_\bullet A(\mathbf{r}) \exp[jk\boldsymbol{\alpha}_p \cdot \mathbf{r} + j\phi(\mathbf{r}, t)]. \quad (4)$$

and the $-$ superscript denotes that this field is upstream of the coronagraph. Since we assume that the planetary light is not effected by the coronagraph, this notation is omitted for u_p .

To model the effect of a the coronagraph in the optical system, we use the formalism of Sauvage et al. (2010), in which “the perfect coronagraph is always defined as an optical device that subtracts a centered Airy pattern from the electromagnetic field.” In the pupil plane downstream of the coronagraph, the stellar field is given by

$$\begin{aligned} u_s(\mathbf{r}, t) &= u_s^-(\mathbf{r}, t) - u_* \eta(t) A(\mathbf{r}) \\ &= u_* \{A(\mathbf{r}) \exp[j\phi(\mathbf{r}, t)] - \eta(t) A(\mathbf{r})\} , \end{aligned} \quad (5)$$

$$(6)$$

where $\eta(t)$ is the complex number ($\|\eta(t)\| < 1$) that minimizes the total energy transmitted by the coronagraph, $\int u_s(\mathbf{r}, t) u_s^*(\mathbf{r}, t) d^2\mathbf{r}$. It is easy to show that

$$\eta(t) = \frac{\int d^2\mathbf{r} A(\mathbf{r}) A^*(\mathbf{r}) \exp[-j\phi_r(\mathbf{r}, t)]}{\int d^2\mathbf{r} A(\mathbf{r}) A^*(\mathbf{r})} \quad (7)$$

where the $*$ superscript indicates complex conjugation, and the $\phi_u(\mathbf{r})$ has been ignored as it has little consequence here. Note that as $\phi(\mathbf{r}, t) \rightarrow 0$, $\eta(t) \rightarrow 1$, implying the extinction of all emission along the telescope’s optical axis, which is the defining characteristic of a perfect coronagraph.

Under Fraunhofer diffraction, the pupil-plane fields u_p and u_s lead to the following post-coronagraph, image-plane fields for the planet and star:

$$v_p(\boldsymbol{\rho}, t) = u_\bullet \int d^2\mathbf{r} A(\mathbf{r}) \exp j \left[-\frac{k}{f} (\boldsymbol{\rho} - f\boldsymbol{\alpha}_p) \cdot \mathbf{r} + \phi_r(\mathbf{r}, t) \right] , \quad (8)$$

$$v_s(\boldsymbol{\rho}, t) = u_* \int d^2\mathbf{r} A(\mathbf{r}) \exp \left[-j\frac{k}{f} \boldsymbol{\rho} \cdot \mathbf{r} \right] \left\{ \exp[j\phi(\mathbf{r}, t)] - \eta(t) \right\} \quad (9)$$

where $\boldsymbol{\rho}$ is the 2D image plane coordinate, f is the effective focal length, and $\phi_u(\mathbf{r})$ has been dropped from Eq. (8), as the planetary light scattered by the static aberrations is not important. The intensity in the image plane is given by the incoherent sum of the planetary and stellar fields:

$$I(\boldsymbol{\rho}, t) = I_s(\boldsymbol{\rho}, t) + I_p(\boldsymbol{\rho}, t) , \quad (10)$$

where $I_p(\boldsymbol{\rho}, t) \equiv v_p(\boldsymbol{\rho}, t) v_p^*(\boldsymbol{\rho}, t)$ and $I_s(\boldsymbol{\rho}, t) = v_s(\boldsymbol{\rho}, t) v_s^*(\boldsymbol{\rho}, t)$. The planetary intensity is given by:

$$\begin{aligned} I_p(\boldsymbol{\rho}, t) &= u_\bullet^2 \int d^2\mathbf{r} \int d^2\mathbf{r}' A(\mathbf{r}) A^*(\mathbf{r}') \times \\ &\quad \exp j \left[\frac{k}{f} (\boldsymbol{\rho} - f\boldsymbol{\alpha}_p) \cdot (\mathbf{r}' - \mathbf{r}) + \phi_r(\mathbf{r}, t) - \phi_r^*(\mathbf{r}', t) \right] . \end{aligned} \quad (11)$$

The star’s intensity is given by:

$$I_s(\boldsymbol{\rho}, t) = u_*^2 \int d^2\mathbf{r} \int d^2\mathbf{r}' A(\mathbf{r}) A^*(\mathbf{r}') \exp \left[j \frac{k}{f} \boldsymbol{\rho} \cdot (\mathbf{r}' - \mathbf{r}) \right] \times \\ \left\{ \eta(t) \eta^*(t) + e^{j[\phi(\mathbf{r}, t) - \phi^*(\mathbf{r}', t)]} - \eta(t) e^{-j\phi^*(\mathbf{r}', t)} - \eta^*(t) e^{j\phi(\mathbf{r}, t)} \right\}, \quad (12)$$

where we remind the reader that $\phi(\mathbf{r}, t) = \phi_r(\mathbf{r}, t) + \phi_u(\mathbf{r})$. Sauvage et al. (2010) obtained an expression equivalent to Eq. (12), except their analysis also included aberrations downstream of the coronagraph. As Sauvage et al. (2010) were primarily concerned with long exposure images, they took the time average of Eq. (12), which eliminates $\phi_r(\mathbf{r}, t)$ in favor of structure functions of the AO residual.

2.0.1. multiple planets and/or extended emission

Equation (11) easily generalizes to the case of extended planetary emission and multiple planets, for which one takes an incoherent sum over all of the various sources. Let $J(\boldsymbol{\alpha})$ be the brightness distribution on the sky (excluding the star), then the generalization of Eq. (11) is:

$$I_p(\boldsymbol{\rho}, t) = \int d^2\boldsymbol{\alpha} J(\boldsymbol{\alpha}) \int d^2\mathbf{r} \int d^2\mathbf{r}' A(\mathbf{r}) A^*(\mathbf{r}') \times \\ \exp j \left[\frac{k}{f} (\boldsymbol{\rho} - f\boldsymbol{\alpha}) \cdot (\mathbf{r}' - \mathbf{r}) + \phi_r(\mathbf{r}, t) - \phi_r^*(\mathbf{r}', t) \right]. \quad (13)$$

Henceforth, the double integral over \mathbf{r} and \mathbf{r}' in Eq. (11) will be called the *planetary intensity kernel*.

2.0.2. modulation of planetary vs. off-axis stellar emission

At the planet location in the image plane, $\boldsymbol{\rho} = f\boldsymbol{\alpha}_p$, consider a 1st order Taylor expansion of the exponential in Eq. (8), which gives:

$$v_p(f\boldsymbol{\alpha}_p, t) \approx u_\bullet \int d^2\mathbf{r} A(\mathbf{r}) [1 + j\phi_r(\mathbf{r}, t)] = u_\bullet \int d^2\mathbf{r} A(\mathbf{r}), \quad (14)$$

where the equality makes use of Eq. (2). Thus, to first order, the planetary field isn’t modulated by the temporal variation of the AO residual phase, and the intensity has no terms that are linear in ϕ_r . Temporal variability in the intensity is due to the higher order

terms in the expansion. In contrast, at the point $\boldsymbol{\rho} = f\boldsymbol{\alpha}_p$, Taylor expansion of the second exponential in Eq. (9) yields:

$$v_s(f\boldsymbol{\alpha}_p, t) \approx u_* \int d^2\mathbf{r} A(\mathbf{r}) \exp[jk\boldsymbol{\alpha}_p \cdot \mathbf{r}] \left[1 - \eta(t) + j\phi_r(\mathbf{r}, t) + j\phi_u(\mathbf{r})\right]. \quad (15)$$

One can see that Eq. (15) indicates that the field should be greatly modulated by the residual atmospheric fluctuations at the location of the planet. The key differences in the temporal behavior between the planetary (sometimes called “on-axis”) case [Eq. (14)], and the stellar (sometimes called “off-axis”) case [Eq. (15)] is due to the spatially oscillating $\exp(-jk\boldsymbol{\alpha}_p \cdot \mathbf{r})$ factor inside the integrand, and the fact that η is a function of time. Fig. 2 gives an example, taken from Experiment 1 in Sec. 4, of the difference in the planetary vs. stellar emission at the same point in the image plane. This stellar emission is enhanced by a static aberration with the spatial frequency corresponding the planetary position. Fig. 3 shows histograms of the planetary intensity (top) and the stellar intensity (bottom) from the same time series. The positive skewness of stellar distribution and the negative one of the planetary distribution was noted by Gladysz et al. (2010), who proposed using these properties to separate exoplanet emission from the stellar speckle.

The differences between the planetary and stellar modulation implied by (8) and Eqs. (9) or Eqs. (14) and (15) hint that short exposures may provide a means to discriminate between the planetary emission and speckle from the star. Thus, one would expect that the WFS estimate of $\phi_r(\mathbf{r}, t)$ should provide some additional means to separate the planetary emission from the speckle.

2.1. Series expansion of the QS aberrations

Our problem requires estimation of the static aberrations, which is less difficult when they can be assumed small enough for the following linearization to be valid:

$$\exp[j\phi_u(\mathbf{r})] \approx 1 + j\phi_u(\mathbf{r}). \quad (16)$$

This is not particularly stringent, as one expects that static errors should satisfy $||\phi_u(\mathbf{r})|| \ll 1$ in a good optical system. Note that $e^{j\phi_r(\mathbf{r}, t)}$ is not linearized in this paper. Calculating the total intensity from Eq. (10) using Eqs. (8), (12), and (16) yields:

$$\begin{aligned} I(\boldsymbol{\rho}, t) = & I_p(\boldsymbol{\rho}, t) + \mathcal{A}(\boldsymbol{\rho}, t) + (\mathcal{B} \circ \phi_u^*)(\boldsymbol{\rho}, t) + \\ & (\mathcal{B}^* \circ \phi_u)(\boldsymbol{\rho}, t) + (\mathcal{C} \circ [\phi_u, \phi_u^*])(\boldsymbol{\rho}, t) \end{aligned} \quad (17)$$

where the \circ symbol indicates composition. Of course, this equation may be generalized to include extended objects and/or multiple planets by replacing the first term with Eq. (13).

The linearization in Eq. (16) applied to Eq. (12), creates three types of terms: those that do not depend on ϕ_u , those that are linear in ϕ_u and those that are quadratic in ϕ_u . These terms are represented, respectively, by the \mathcal{A} , \mathcal{B} , and \mathcal{C} terms in Eq. (17). Before giving formulae for these operators it is useful to define the kernel function:

$$G(\mathbf{r}, \mathbf{r}'; \boldsymbol{\rho}) \equiv A(\mathbf{r})A^*(\mathbf{r}') \exp \left[-j \frac{k}{f} \boldsymbol{\rho} \cdot (\mathbf{r} - \mathbf{r}') \right], \quad (18)$$

which has the useful symmetry property: $G(\mathbf{r}, \mathbf{r}'; \boldsymbol{\rho}) = G^*(\mathbf{r}', \mathbf{r}; \boldsymbol{\rho})$.

$$\begin{aligned} \mathcal{A}(\boldsymbol{\rho}, t) &= u_*^2 \int d^2\mathbf{r} \int d^2\mathbf{r}' G(\mathbf{r}, \mathbf{r}'; \boldsymbol{\rho}) \left\{ \eta(t)\eta^*(t) + \exp j[\phi_r(\mathbf{r}, t) - \phi_r^*(\mathbf{r}', t)] \right. \\ &\quad \left. - \eta(t) \exp[-j\phi_r^*(\mathbf{r}', t)] - \eta^*(t) \exp[j\phi_r(\mathbf{r}, t)] \right\} \end{aligned} \quad (19)$$

$$\begin{aligned} (\mathcal{B} \circ \phi_u^*)(\boldsymbol{\rho}, t) &= u_*^2 \int d^2\mathbf{r} \int d^2\mathbf{r}' G^*(\mathbf{r}, \mathbf{r}'; \boldsymbol{\rho}) \phi_u^*(\mathbf{r}) \times \\ &\quad \left\{ j\eta(t) \exp[-j\phi_r^*(\mathbf{r}, t)] - j \exp j[\phi_r(\mathbf{r}', t) - \phi_r^*(\mathbf{r}, t)] \right\} \end{aligned} \quad (20)$$

$$\begin{aligned} (\mathcal{B}^* \circ \phi_u)(\boldsymbol{\rho}, t) &= u_*^2 \int d^2\mathbf{r} \int d^2\mathbf{r}' G(\mathbf{r}, \mathbf{r}'; \boldsymbol{\rho}) \phi_u(\mathbf{r}) \times \\ &\quad \left\{ -j\eta^*(t) \exp[j\phi_r(\mathbf{r}, t)] + j \exp j[\phi_r(\mathbf{r}, t) - \phi_r^*(\mathbf{r}', t)] \right\} \end{aligned} \quad (21)$$

$$(\mathcal{C} \circ [\phi_u, \phi_u^*])(\boldsymbol{\rho}, t) = u_*^2 \int d^2\mathbf{r} \int d^2\mathbf{r}' G(\mathbf{r}, \mathbf{r}'; \boldsymbol{\rho}) \phi_u(\mathbf{r}) \phi_u^*(\mathbf{r}') \exp j[\phi_r(\mathbf{r}, t) - \phi_r^*(\mathbf{r}', t)] \quad (22)$$

In Eq. (17), the \mathcal{A} term is due to the atmospheric residual speckles, the \mathcal{C} term is due to the static aberrations, and the \mathcal{B} terms are due to the mixing of these two effects, the so-called “pinned speckle” (Bloemhof 2004). Note that when $\phi_u = 0$, $I_s(\boldsymbol{\rho}, t) = \mathcal{A}(\boldsymbol{\rho}, t)$. While all of the integrals in Eqs.(19) through (22) can be separated to integrate over \mathbf{r} and \mathbf{r}' independently, the form given here is more conducive to presentation.

To make estimation of the QS aberrations tractable, we assume a finite expansion for $\phi_u(\mathbf{r})$

$$\phi_u(\mathbf{r}) = \sum_{k=1}^K a_k \psi_k(\mathbf{r}) \quad (23)$$

where K is the number of terms required and $\{\psi_k(\mathbf{r})\}$ are basis functions on which the static aberrations can be represented. Orthogonality of the $\{\psi_k(\mathbf{r})\}$ will not be assumed, allowing considerable freedom in the form of the expansion. For convenience, we put the quantities $\{a_k\}$ into a $1 \times K$ (column) vector \mathbf{a} . Substituting Eq. (23) into Eq. (17) gives three types of terms, those that are independent of \mathbf{a} , linear in \mathbf{a} , and quadratic in \mathbf{a} :

$$I(\boldsymbol{\rho}, t) = u_{\bullet}^2 i_p(\boldsymbol{\rho}, t) + \mathcal{A}(\boldsymbol{\rho}, t) +$$

$$\mathbf{a}^H \mathbf{b}(\boldsymbol{\rho}, t) + \mathbf{b}^H(\boldsymbol{\rho}, t) \mathbf{a} + \mathbf{a}^H \mathbf{C}(\boldsymbol{\rho}, t) \mathbf{a}, \quad (24)$$

where the ^H superscript indicates the transpose and complex conjugate (Hermitian conjugate), $i_p(\boldsymbol{\rho}, t) \equiv I_p(\boldsymbol{\rho}, t)/u_\bullet^2$ is the normalized planetary brightness. The column vector $\mathbf{b}(\boldsymbol{\rho}, t)$ has K components, and $\mathbf{C}(\boldsymbol{\rho}, t)$ is a $K \times K$ matrix. Thus, for fixed $(\boldsymbol{\rho}, t)$, $\mathbf{a}^H \mathbf{b}(\boldsymbol{\rho}, t)$ is the scalar product of the two complex vectors. Similarly, $\mathbf{C}(\boldsymbol{\rho}, t) \mathbf{a}$ is the standard matrix-vector multiplication, with $\mathbf{a}^H \mathbf{C}(\boldsymbol{\rho}, t) \mathbf{a}$ resulting in a scalar. Using Eqs. (20), (22) and (23), the components of \mathbf{b} and \mathbf{C} are given by:

$$[\mathbf{b}(\boldsymbol{\rho}, t)]_k = u_*^2 \int d^2 \mathbf{r} \int d^2 \mathbf{r}' G^*(\mathbf{r}, \mathbf{r}'; \boldsymbol{\rho}) \psi_k^*(\mathbf{r}) \times \left\{ j\eta(t) \exp[-j\phi_r^*(\mathbf{r}, t)] - j \exp j[\phi_r(\mathbf{r}', t) - \phi_r^*(\mathbf{r}, t)] \right\} \quad (25)$$

$$[\mathbf{C}(\boldsymbol{\rho}, t)]_{kl} = u_*^2 \int d^2 \mathbf{r} \int d^2 \mathbf{r}' G(\mathbf{r}, \mathbf{r}'; \boldsymbol{\rho}) \psi_k(\mathbf{r}) \psi_l^*(\mathbf{r}') \times \exp \left\{ j\phi_r(\mathbf{r}, t) - j\phi_r^*(\mathbf{r}', t) \right\}. \quad (26)$$

Note that Eqs. (25) and (26) are separable and can be computed rapidly with fast Fourier transforms, as can $\mathcal{A}(\boldsymbol{\rho}, t)$.

3. Detection/Estimation Problem

The problem of detecting and estimating the planetary emission in the framework presented here can be posed as separating the planetary and stellar emission given noisy measurements of $I(\boldsymbol{\rho}, t)$ and the WFS data, summarized as the estimate of the AO residual $\hat{\phi}_r(\mathbf{r}, t)$. It follows that using the WFS to estimate $\phi_r(\mathbf{r}, t)$ is a key aspect of the proposed methodology.¹ While some current WFS' estimate other quantities, such as $\nabla \phi_r(\mathbf{r}, t)$ in the case of Shack-Hartmann sensors, estimating $\phi_r(\mathbf{r}, t)$ from the WFS data is always possible with additional processing. Optimal estimation of $\phi_r(\boldsymbol{\rho}, t)$ with the maximum likelihood method is discussed in (Barrett et al. 2007) and (Béchet et al. 2009).

The most general case allows the planetary emission to be a function of the sky-angle $\boldsymbol{\alpha}$, and then the problem would be estimate the spatial function $J(\boldsymbol{\alpha})$ simultaneously with the QS aberration coefficients \mathbf{a} , a problem which falls under the category of estimation theory.

¹Alternatively, one may also consider skipping the step of building the estimate $\hat{\phi}_r(\mathbf{r}, t)$ and instead finding optimal estimators for \mathcal{A} , \mathcal{B} , and \mathcal{C} given the WFS data.

In contrast, the problem of trying to decide whether or not there is planetary emission falls under the regime of detection theory. Considering the problem of exoplanet detection, Caucci et al. (2007) simulated the scanning Hotelling observer, in which one “scans” the image, i.e., one considers the probability of detection of a source at one point $\boldsymbol{\alpha}_k$ at a time. In Caucci et al. (2009), they generalized their previous analysis to include a time series of images. The possibility of multiple planets considerably complicates scanning observer framework and it is not suited for estimation of extended emission. The, perhaps naïve, first step approach in this manuscript is to assume that extended emission or other planets at locations other than $\boldsymbol{\alpha}_p$ are weak enough not to significantly influence the estimate of u_{\bullet}^2 and the error bar on this quantity, the numerical examples in Sec. 4 support this notion. If this estimate is non-zero by several error bars, then it can be considered a detection. Of course, a scanning approach may be applied for a series of candidate angles. In any case, short exposures and WFS data could also be incorporated into a scanning observer framework.

3.1. Linear System Formulation

Here we put Eq. (24) into the canonical form for linear systems, $\mathbf{y} = \mathbf{H}\mathbf{x}$, where \mathbf{y} represents the “observation” vector, \mathbf{x} is the vector of unknowns and \mathbf{H} is the system model or “data,” as it is sometimes called in the statistics literature.

While Eq. (24) has only $K + 1$, unknowns, it is nonlinear due to the quadratic term, $\mathbf{a}^H \mathbf{C}(\boldsymbol{\rho}, t) \mathbf{a}$, which is likely to introduce numerical difficulties. In exchange for creating an additional set of unknowns, one may remove this nonlinearity. The new K^2 unknowns are the quantities $\{a_k a_l^*\}$, which are placed into the $1 \times K^2$ vector \mathbf{d} . Similarly rearranging the matrix elements $\mathbf{C}(\boldsymbol{\rho}, t)$ into the $K^2 \times 1$ vector $\mathbf{c}^H(\boldsymbol{\rho}, t)$, one obtains:

$$\mathbf{a}^H \mathbf{C}(\boldsymbol{\rho}, t) \mathbf{a} = \mathbf{c}^H(\boldsymbol{\rho}, t) \mathbf{d}. \quad (27)$$

Consider a template with N spatial locations $\{\boldsymbol{\rho}_1, \dots, \boldsymbol{\rho}_N\}$, and take $\boldsymbol{\rho}_1 = f\boldsymbol{\alpha}_p$ to be the location at which we desire to know whether or not there is a planet present and how bright it might be. This selection of points forms the spatial template. We assume that the science camera exposures are simultaneous with the output of the AO system wavefront measurements, with T exposures taken at times $\{t_1, \dots, t_T\}$. These exposure times form the temporal template. Thus, there are NT observations to be placed into the vector:

$$\mathbf{y} = \begin{bmatrix} \mathbf{y}_1 \\ \vdots \\ \mathbf{y}_T \end{bmatrix}, \quad (28)$$

where the $\{\mathbf{y}_i\}$ vectors (one for each exposure) are given by:

$$\mathbf{y}_i = \begin{bmatrix} I(\boldsymbol{\rho}_1, t_i) \\ \vdots \\ I(\boldsymbol{\rho}_N, t_i) \end{bmatrix} - \begin{bmatrix} \mathcal{A}(\boldsymbol{\rho}_1, t_i) \\ \vdots \\ \mathcal{A}(\boldsymbol{\rho}_N, t_i) \end{bmatrix}. \quad (29)$$

Similarly, the (column) vector $\mathbf{x} = [u_{\bullet}^2, \mathbf{a}^T, \mathbf{a}^H, \mathbf{d}^T]^T$, where T indicates transposition (without complex conjugation). Following the same notation scheme,

$$\mathbf{H} = \begin{bmatrix} \mathbf{H}_1 \\ \vdots \\ \mathbf{H}_T \end{bmatrix}, \quad (30)$$

where the individual matrices $\{\mathbf{H}_i\}$ have the structure:

$$\mathbf{H}_i = \begin{bmatrix} i_p(\boldsymbol{\rho}_1, t_i) & \mathbf{b}^T(\boldsymbol{\rho}_1, t_i) & \mathbf{b}^H(\boldsymbol{\rho}_1, t_i) & \mathbf{c}^H(\boldsymbol{\rho}_1, t_i) \\ \vdots & \vdots & \vdots & \vdots \\ i_p(\boldsymbol{\rho}_N, t_i) & \mathbf{b}^T(\boldsymbol{\rho}_N, t_i) & \mathbf{b}^H(\boldsymbol{\rho}_N, t_i) & \mathbf{c}^H(\boldsymbol{\rho}_1, t_i) \end{bmatrix} \quad (31)$$

Then, under the linear formulation, the estimation problem is to find the values of u_{\bullet}^2 , \mathbf{a} and \mathbf{d} which best satisfy:

$$\mathbf{y} = \mathbf{H} \begin{bmatrix} u_{\bullet}^2 \\ \mathbf{a} \\ \mathbf{a}^* \\ \mathbf{d} \end{bmatrix} \quad (32)$$

Note that the scale of the linear computation may not be especially daunting, as there are only $K^2 + 2K + 1$ unknowns, which is much less than the NT data points. For example, the $\mathbf{H}^H \mathbf{H}$ only has $K^2 + 2K + 1$ singular values.

When considering spatially extended planetary emissions, the \mathbf{x} vector is expanded so that u_{\bullet}^2 is replaced a column vector representing the extended emissions and $i_p(\boldsymbol{\rho}_1, t)$ is replaced by a matching row vector accounting for the convolution with the planetary intensity kernel [cf. Eq. (13)].

If \mathbf{a} is complex, then the estimate can be improved by demanding consistency between the estimates of \mathbf{a} and \mathbf{a}^* , or, re-expressing the system in terms of real and imaginary parts. Of course, if \mathbf{a} is assumed to be real, meaning static errors only affect the phase, not the amplitude, \mathbf{x} simplifies to $\mathbf{x} = [u_{\bullet}^2, \mathbf{a}^T, \mathbf{d}^T]^T$, and the 2nd and 3rd columns of \mathbf{H} are summed together to form a single column. In addition, a positivity constraint may be applied to the planetary emission component.

3.2. Quadratic System Formulation

The linear formulation may improve the computational possibilities by providing an excellent “warm start” to a calculation that takes the quadratic relationships into account. It may be useful to note that given linear estimates of \mathbf{a} and \mathbf{d} , $\hat{\mathbf{a}}$ and $\hat{\mathbf{d}}$, and their error covariances $C_{\mathbf{aa}}$, $C_{\mathbf{ad}}$ and $C_{\mathbf{dd}}$, in a second computation, one could improve the estimates of \mathbf{a} by using the knowledge that each component of \mathbf{d} is equal to $a_i a_j^*$ for a particular choice of i and j .

The objective of this section is to write the system in the form $\mathbf{y} = \mathbf{H}'\mathbf{x}' + \mathbf{Q}(\mathbf{x}')$, where \mathbf{Q} is the quadratic term. The vector \mathbf{y} is the same in both the linear and quadratic formulations. The quadratic version of \mathbf{H} , \mathbf{H}' is the same as \mathbf{H} , except with the final column removed:

$$\mathbf{H}'_i = \begin{bmatrix} i_p(\boldsymbol{\rho}_1, t_i) & \mathbf{b}^T(\boldsymbol{\rho}_1, t_i) & \mathbf{b}^H(\boldsymbol{\rho}_1, t_i) \\ \vdots & \vdots & \vdots \\ i_p(\boldsymbol{\rho}_N, t_i) & \mathbf{b}^T(\boldsymbol{\rho}_N, t_i) & \mathbf{b}^H(\boldsymbol{\rho}_N, t_i) \end{bmatrix}, \quad (33)$$

so that $\mathbf{H}' = [\mathbf{H}'_1, \dots, \mathbf{H}'_T]^T$. Similarly, $\mathbf{x}' = [u_\bullet^2, \mathbf{a}^T, \mathbf{a}^H]^T$.

To put the quadratic term in a form suitable for digital computation, we first note for each of the NT points in the spatio-temporal template we need to calculate the scalar value of $\mathbf{a}^H \mathbf{C}(\boldsymbol{\rho}, t) \mathbf{a}$, which is achieved with the following formulation:

$$\mathbf{Q}(\mathbf{a}) \equiv (\mathbf{1}_{NT} \otimes \mathbf{a}^H) \begin{bmatrix} \mathbf{C}(\boldsymbol{\rho}_1, t_1) \\ \vdots \\ \mathbf{C}(\boldsymbol{\rho}_N, t_1) \\ \mathbf{C}(\boldsymbol{\rho}_1, t_2) \\ \vdots \\ \mathbf{C}(\boldsymbol{\rho}_N, t_T) \end{bmatrix} \mathbf{a} \quad (34)$$

where $\mathbf{1}_{NT}$ is the row vector $[1, \dots, 1]$ with NT components, and \otimes is the Kronecker matrix product. This Kronecker product creates a large row vector with NT copies of the row vector \mathbf{a}^H . Then, the quadratic variant of the problem can be stated as finding the u_\bullet^2 and \mathbf{a} which

best satisfy:

$$\mathbf{y} = \mathbf{H}' \begin{bmatrix} u_{\bullet}^2 \\ \mathbf{a} \\ \mathbf{a}^* \end{bmatrix} + (\mathbf{1}_{NT} \otimes \mathbf{a}^H) \begin{bmatrix} \mathbf{C}(\boldsymbol{\rho}_1, t_1) \\ \vdots \\ \mathbf{C}(\boldsymbol{\rho}_N, t_1) \\ \mathbf{C}(\boldsymbol{\rho}_1, t_2) \\ \vdots \\ \mathbf{C}(\boldsymbol{\rho}_N, t_T) \end{bmatrix} \mathbf{a}. \quad (35)$$

3.3. Uncertainty Propagation

This section considers uncertainty propagation within the linear formulation of the problem, $\mathbf{y} = \mathbf{H}\mathbf{x}$ provided in Sec. 3.1. The quadratic version of the problem, formulated in Sec. 3.2, will have smaller uncertainties due to the much smaller number of variables to estimate, but determining them requires more specialized mathematical procedures than the linear case.

This section will assume that NT is much greater than the number of parameters to be estimated. In practice this will be satisfied, as millisecond exposure times will produce a lot of data. For example, with a spatial template consisting of 1000 pixels, and exposure times of 10^{-3} seconds, one hour of observation gives $NT = 3.6 \times 10^6$ data points. If the QS aberration expansion has, say, 20 terms, the \mathbf{x} vector will have 441 components, and the linear problem can be considered with the framework of least-squares.

The first term in \mathbf{y} , the observed intensity I , inherits its statistical properties from noise in the observations (most likely dominated by Poisson counting noise and detector read noise), which are treated with relative ease. However, it is of critical importance to bear in mind that the errors in $\hat{\phi}_r(\mathbf{r}, t)$ will cause uncertainties in both \mathbf{y} and \mathbf{H} which must be propagated to \mathbf{x} [cf. Eqs. (28) and (30)]. Standard least squares is likely to be insufficient, and total least squares (TLS) is a more appropriate analysis framework (Van Huffel and Vanderwalle 1991).

One of the useful properties of the short-exposure framework presented here, which is not shared by LOCI and other currently operational processing methods, is that increasing observation time reduces the covariance of $\hat{\mathbf{x}}$ as $1/T$. In contrast, the other algorithms do not improve their estimates of the PSF as one is the observing time increases. This can be shown for the simple case of a perfect WFS, for which $\hat{\phi}_r(\mathbf{r}, t) = \phi_r(\mathbf{r}, t)$. This implies that \mathbf{H} is known exactly, as is $\mathcal{A}(\boldsymbol{\rho}, t)$, so that the only uncertainty remaining comes from the measurement noise in $I(\boldsymbol{\rho}, t)$, which is manifested in \mathbf{y} according to Eq. (28). Consider

a spatial template of N detector pixels and assume that the measurement noise of each exposure has an $N \times N$ diagonal covariance matrix Σ_N , which is the same for each of the T exposures. Then, the total covariance matrix for all of the NT data points is given by large diagonal matrix $\Sigma = \mathbf{I}_T \otimes \Sigma_N$, where \mathbf{I}_T is the T -by- T identity matrix, and log-likelihood function is therefore given by:

$$\ln L(\mathbf{x}|\mathbf{y}) \propto -(\mathbf{y} - \mathbf{H}\mathbf{x})^H \Sigma^{-1} (\mathbf{y} - \mathbf{H}\mathbf{x}). \quad (36)$$

This likelihood is maximized by $\hat{\mathbf{x}} = (\mathbf{H}^H \Sigma^{-1} \mathbf{H})^{-1} \mathbf{H}^H \Sigma^{-1} \mathbf{y}$, and the covariance of $\hat{\mathbf{x}}$ is given by the $(K^2 + 2K + 1)$ -by- $(K^2 + 2K + 1)$ matrix:

$$\Sigma_{\mathbf{x}} = (\mathbf{H}^H \Sigma^{-1} \mathbf{H})^{-1} = \left(\sum_{i=1}^T \mathbf{H}_i^H \Sigma_N^{-1} \mathbf{H}_i \right)^{-1}. \quad (37)$$

Now, each of the matrices $(\mathbf{H}_i^H \Sigma_N^{-1} \mathbf{H}_i)$ is positive semi-definite, and the trace (which is the sum eigenvalues) of the sum $\sum_{i=1}^T (\mathbf{H}_i^H \Sigma_N^{-1} \mathbf{H}_i)$ must increase, on average, linearly with the number of exposures T . Furthermore, since each of the \mathbf{H}_i is a manifestation of an independent, random phase screen $\phi_r(\mathbf{r}, t_i)$, matrices associated with exposures taken at two times t_k and t_l are unlikely to have a common null space so that, on average, the smallest eigenvalue of the sum increases linearly with T , on average, thus, justifying the approximation:

$$\left(\sum_{i=1}^T \mathbf{H}_i^H \Sigma_N^{-1} \mathbf{H}_i \right)^{-1} \approx (T \langle \mathbf{H}_i^H \Sigma_N^{-1} \mathbf{H}_i \rangle)^{-1}, \quad (38)$$

where the brackets $\langle \rangle$ indicates ensemble average over the statistics of the AO residual. Thus, it is clear that $\Sigma_{\mathbf{x}}$ is proportional to $1/T$. While generalization of this proof to the case in which \mathbf{H} also has uncertainty and its own covariance matrix is likely to be substantially more difficult, it seems that this basic result is unlikely to change.

4. Numerical Simulations

This section explores some of the concepts described above with numerical simulation. In these experiments, residual phase data taken by the WFS on the AEOS Adaptive Optics System (Roberts & Neyman 2002), interpolated onto 256×256 grid, was used as $\phi_r(\mathbf{r}, t)$. In order to keep these calculations as simple as possible, wavefront sensor error was not included, so the AO residual was exactly given by interpolated AEOS data. AEOS has 941 actuators and the wavefront data utilized here corresponds to a sampling rate of 10^{-3} s. The AEOS sensing wavelength was 850 nm and these numerical exercises assumed a science

camera operating at $2.2\ \mu$ that samples at exactly the rate as the WFS (with no delay). The residual phase value was converted from the 850 nm value to the $2.2\ \mu$ by assuming that the optical path length difference is independent of wavelength, so that the residual phase in radians simply scales inversely with the wavelength. These experiments processed either 1 s or 4 s of AEOS data, with different, but known, wavefronts. Figure 4 shows the $2.2\ \mu$ Strehl ratio for all 4000 exposures, given by $|\eta(t)|$ in Eq. (7). Also depicted on the same graph is the fraction of the stellar emission removed by the coronagraph. At best, it removes about 95% of the stellar emission and much less when the Strehl ratio falls. The 850 nm Strehl ratios are much smaller and are not shown here.

The static aberrations in these experiments included 11 terms in the expansion shown in Eq. (23): Zernike functions numbered 41-50 as well as a sinusoid which places a speckle at pixel locations (120,120), and (138,138). The coefficients $\{a_k\}$ as well as the aberration functions $\{\psi_k\}$ were real, corresponding to phase-only aberrations. The chosen values of $\{a_k\}$ resulted in the aberration function shown in Figure 5. In order to avoid the complications associated with estimation in non-Gaussian noise, Gaussian noise was chosen to behave similarly to the Poisson distribution. Thus, if the (noise-free) intensity was I photons in a millisecond exposure, the “measured” value would be $I + n$, where n was taken from a zero-mean normal distribution with a variance equal to I .

Experiment 1 used 4000 frames and had an average planetary intensity of ~ 0.2 photons/millisecond at pixel (120,120), exactly the location of one of the speckles created by the sinusoidal static aberration. The center of the image was at pixel (129,129), and the average stellar intensity was ~ 9 photons/millisecond at pixel (120,120). The contrast ratio between the planetary and stellar brightness was 10^{-6} . The noise-free stellar brightness, averaged over all 4000 frames, is shown Fig. 6. The speckle due to the sinusoidal component of the static aberrations can be seen at pixel (120,120), exactly the location of the planet. The conjugate point to this speckle is also visible at pixel (138,138). Note that the two conjugate points have different intensities due to other aberrations and the random AO residual and therefore one could not make a good estimate of the planetary intensity by assuming that the two speckles are the same. Also, the planet is much too faint to be visually distinguishable from the stellar image.

The spatial template was a square in the center of the image, ranging from pixels 105 to 153 in each direction, resulting in $49^2 = 2401$ pixels per image. This resulted in the matrix \mathbf{H} having a size of $9,604,000 \times 133$. The intensity of the planet was normalized to 1.0 in the linear system (see Sec. 3.1), and the experiment was run with 9 different realizations of the noise. These 9 runs had a mean estimate of the planetary intensity of 1.01 and a standard deviation of 0.17, which compares favorably to the square-root of the 1-1 element of the

estimate error covariance matrix in Eq. (37) of 0.172. Fig. 7 shows the estimates from one of the runs and the corresponding true values of the linear coefficients $\{a_k\}$. The error bars come from the square-root of the diagonal of the estimator covariance matrix. Similarly, Fig. 8 shows the estimates and true values of the quadratic coefficients $\{a_k a_j^*\}$ (although complex conjugation was not needed since all coefficients were real).

Experiment 2 was the same as experiment 1, except only 1000 exposures were used. This experiment was run with 22 realization of the random noise. The mean estimate of the normalized planetary intensity in these runs was 1.05 and standard deviation was 0.4, comparing favorably to the square-root of the 1-1 element of the estimate error covariance matrix in Eq. (37) of 0.37. Experiment 2 had a standard deviation in the estimates that was about double those of Experiment 1, supporting the contention that the estimate error covariance is inversely proportion to the observation time, as indicated in Eq. (38). The estimates of the linear static aberration coefficients had a variances about twice the variance of those in Experiment 1, and the equivalent to Fig. 7 is visually undistinguishable. The quadratic aberration coefficients had a much larger variance (due to loss of diversity with fewer random phase screens), and the equivalent of Fig. 8 is given in Fig. 9.

Experiment 3 was the same as Experiment 2, except all of the equations and data were summed over all 1000 exposures. The resulting estimates of the planetary emission were useless with a standard deviation more than two orders of magnitude greater than the planetary intensity. This is because the summation destroys the diversity provided by the modulation of the AO residual. Thus, direct incorporation of the WFS data is useless for long exposure imaging.

Experiment 4 was designed to test the algorithm’s stability to planetary emission from angles other than α_p . Ideally, planetary emission at other angles would have a negligible effect on the estimates of both the static aberration coefficients and the planetary emission at α_p . In Experiment 4, the planet was placed at the neighboring pixel (119,119) and the brightness was increased by a factor of 100, reducing the contrast ratio to 1×10^4 , but the same matrix \mathbf{H} from Experiment 2 was used, which had 1000 exposures and assumed any planetary emission is due to pixel (120,120). The ideal result of this experiment would be a planetary intensity estimate of 0 and the correct estimates of the static aberration coefficients. This experiment was run 10 times and the mean estimated planetary intensity at pixel (120,120) was 0.021 (the planetary intensity was normalized to unity) with a standard deviation of 0.0038, in good agreement with estimator error standard deviation of 0.00375. Note that this experiment did not attempt to estimate the planetary emission at pixel (119,119), although generalizing to estimate planetary emission at a number of pixels simultaneously is straightforward, as described in Sec. 2.0.1, at the expense of expanding

the number of unknowns. Importantly, in this experiment, the estimates of the linear static aberration coefficients were almost perfect, nearly as good as in Experiment 2. However, the quadratic coefficient estimates were noisier, as shown in Fig. 10, which should be compared to Fig. 9. The fact that a relatively strong planetary source had only 2.1% “leakage” into the neighboring pixel indicates that the estimation method here is likely to be useful as a scanning detector, in which one evaluates the possibility of planetary emission one pixel at a time. Interestingly, the larger estimator variance of the quadratic coefficients may be useful as a clue that planetary emission from an unaccounted region is present. Of course, this technique can be generalized to simultaneously evaluating a block of pixels and scanning the block, which would make it more robust to contamination from neighboring pixels.

Presumably, utilizing the quadratic formulation of the problem described in Sec. 3.2 would lead to superior results than those reported here, but the difficulties in minimizing the quadratic form in Eq. (35) and in determining the uncertainties in the estimates are left to a later study.

5. Conclusions

This paper describes a powerful method for simultaneously estimating the static aberrations and the planetary emission from millisecond exposures with ground-based stellar coronagraphs. The new and crucial aspect of this work is that the method incorporates the wavefront sensor’s estimate of the AO residual phase to provide much needed diversity in the data. Thus, new and statistically independent information about the planetary emissions and quasi-static aberrations is revealed on the atmospheric clearing time-scale (McIntosh et al. 2005), which is more-or-less the telescope diameter divided by the wind speed. It is this diversity property that allows the covariance of the estimate of the planetary emission and the QS aberrations to decrease linearly with observation time, unlike the methods that are presently utilized, whose estimates of the PSF do not asymptotically improve with increased observation time. While, the random AO residual is an extremely useful source of diversity which can be used to characterize the optical system while simultaneously estimating the planetary emission, a fundamental trade-off is shown in Fig. 4: large AO residual is accompanied by poor rejection of stellar emission by the coronagraph.

While, for the sake of simplicity, the mathematical development provided here ignores aberrations downstream of the coronagraph, assumes an ideal coronagraph and Fraunhofer diffraction, etc., improvements upon these assumptions can be incorporated within the proposed framework of short-exposure estimation. Furthermore, the method given here generalizes to include spectrally resolved data and the diurnal field rotation. E.g., to take

advantage of S spectral channels, one must solve for S planetary intensities simultaneously, but there are still only K independent values characterizing the QS aberrations, since the phase variation scales with wavelength. Similarly, to take advantage of angular diversity, one only has to apply a coordinate transformation before including the additional data.

In order to apply the method proposed here to real data sets a number of challenges must be met. While any practical realization will no doubt have to consider various details, e.g., time differences in the exposures of the WFS and the science camera, the more essential issues include the following:

- Develop detectors with low readout noise so that short exposures are not penalized.
- Provide an expansion of the QS aberrations that is realistic, as per Eq. (23). As there is no requirement that the expansion functions are orthogonal, there is considerable freedom allowed, however, the more terms that are required, the more difficult the estimation task becomes. Any method for estimation of exoplanet intensities, whether with long exposures or short, must do this in some form.
- Provide optimal estimators of AO residual $\phi_r(\boldsymbol{\rho}, t)$ and its error statistics, given the WFS data.
- Given the statistics of the AO residual, determine the bias and variance of the elements of the matrix \mathbf{H} and the atmospheric speckle function $\mathcal{A}(\boldsymbol{\rho}, t)$.
- Given the required statistics on necessary quantities, develop the necessary numerical methods to solve the linear and quadratic formulations and determine the error bars on the solution.

The fundamental limits of the short exposure approach are not easy to determine, as they are set by the accuracy of the various modeling aspects of the coronagraph system, including the reduction of the QS aberrations to a finite set of parameters, as well as the various/bias characteristics of the estimator of the AO residual. In a practical application, these will need to be evaluated with care.

I would like to thank Paul Shearer, Yves Atchade, Jr., Peter Lawson, Jean-Francois Sauvage, Kjethil Dohlen, and Mamadou Ndiaye for discussions that enriched these investigations. I extend special gratitude to Lewis C. Roberts for help with the AEOS data and discussing the manuscript.

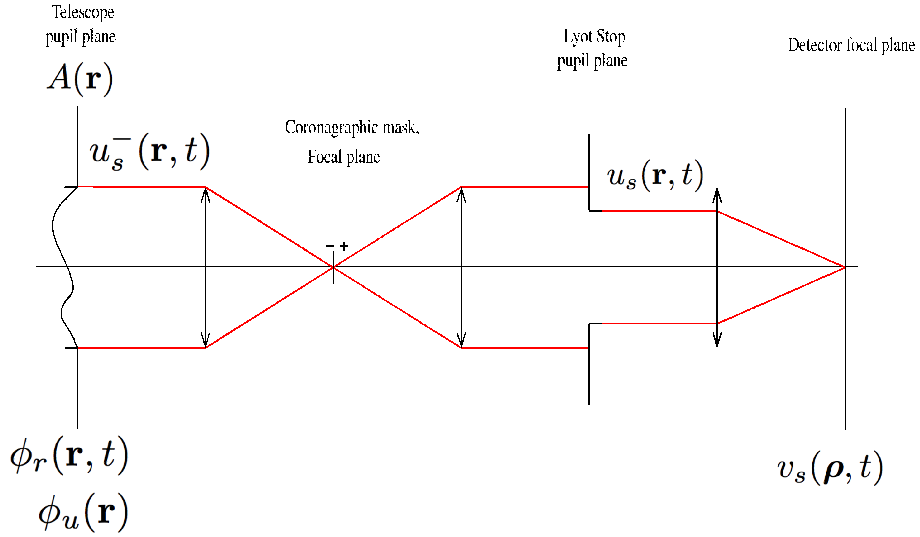


Fig. 1.— (color online) Optical scheme of a coronagraphic imager. The incoming AO residual is $\phi_r(\mathbf{r}, t)$, and the upstream static aberration is denoted $\phi_u(\mathbf{r})$ (downstream static aberrations are not included in this analysis). The pupil plane fields upstream and downstream of the coronagraphic focal plane mask and downstream of the Lyot stop are given by $u_s^-(\mathbf{r}, t)$, and $u_s(\mathbf{r}, t)$, respectively. The aperture function $A(\mathbf{r})$ accounts for both the telescope aperture and the Lyot stop. From Sauvage et al. (2010).

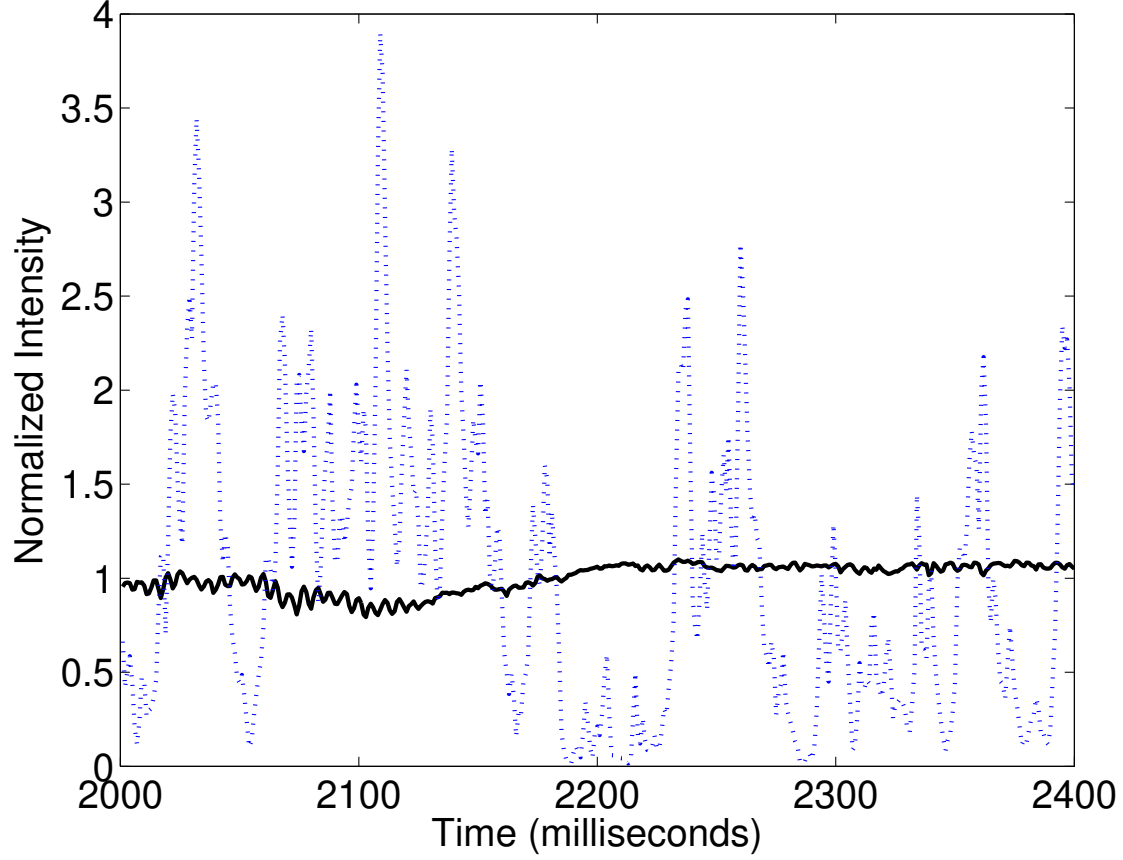


Fig. 2.— (color online) The black solid line shows a portion of the time-series of the temporal variation of the planetary intensity from the Experiment 1 in Sec. 4. The dashed blue line shows the stellar intensity at the planet’s location in the image plane, taken from the same numerical experiment. Both the planetary and stellar intensity are normalized to have a mean of unity in this figure. The stellar intensity is enhanced by sinusoidal static aberration at the spatial frequency corresponding to planet’s location (cf. Fig. 5).

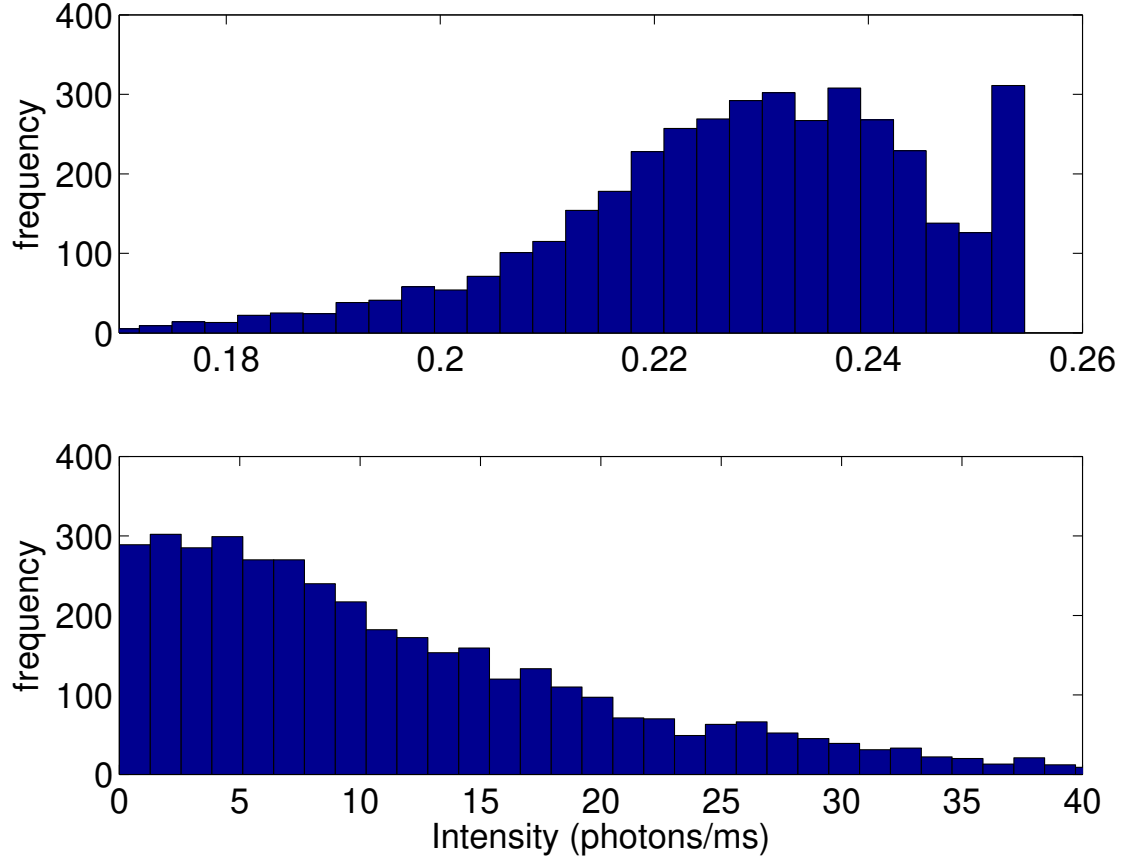


Fig. 3.— (color online) Histograms of the planetary intensity (top) and the stellar intensity (bottom) from the full time series excerpted in Fig. 2. These distributions do not correspond to simple analytical forms, but exhibit the negative (top) and positive skewness discussed in Gladysz et al. (2010).

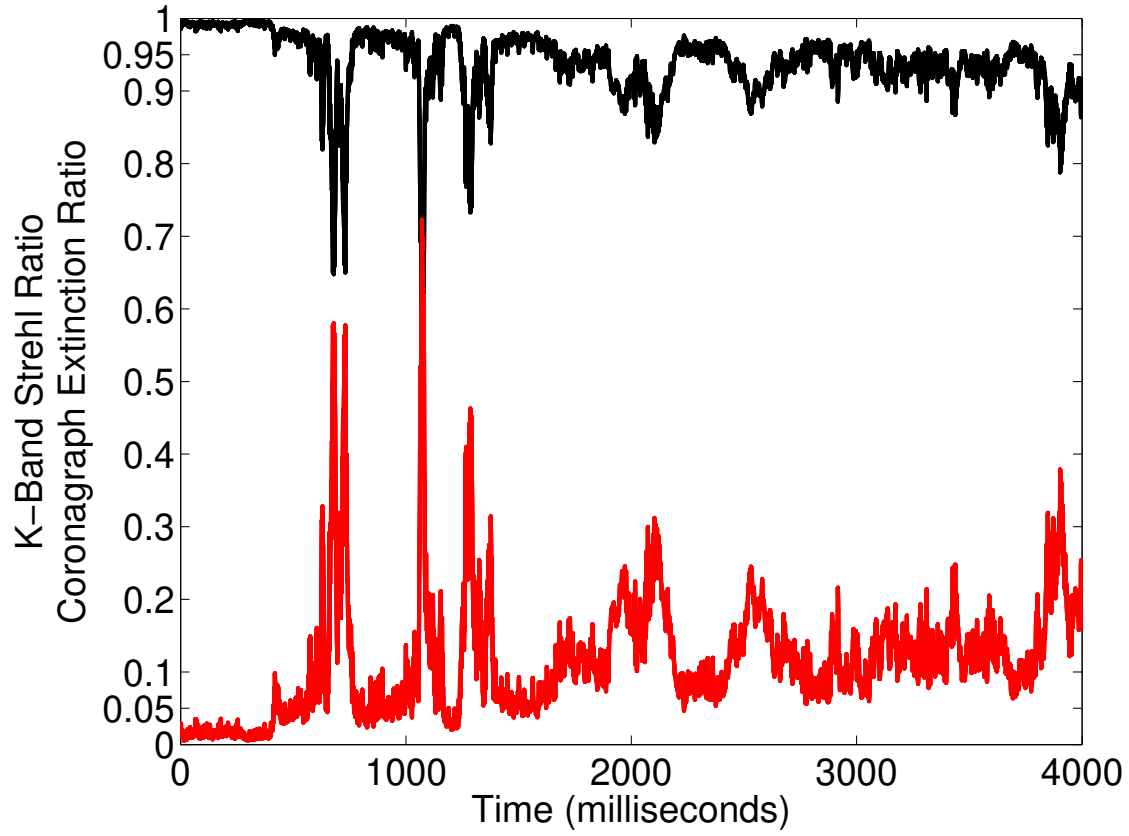


Fig. 4.— (color online) The 2.2μ The black curve shows Strehl ratio for the Experiment 1, and the red curve below shows the fraction of light removed by the ideal coronagraph.

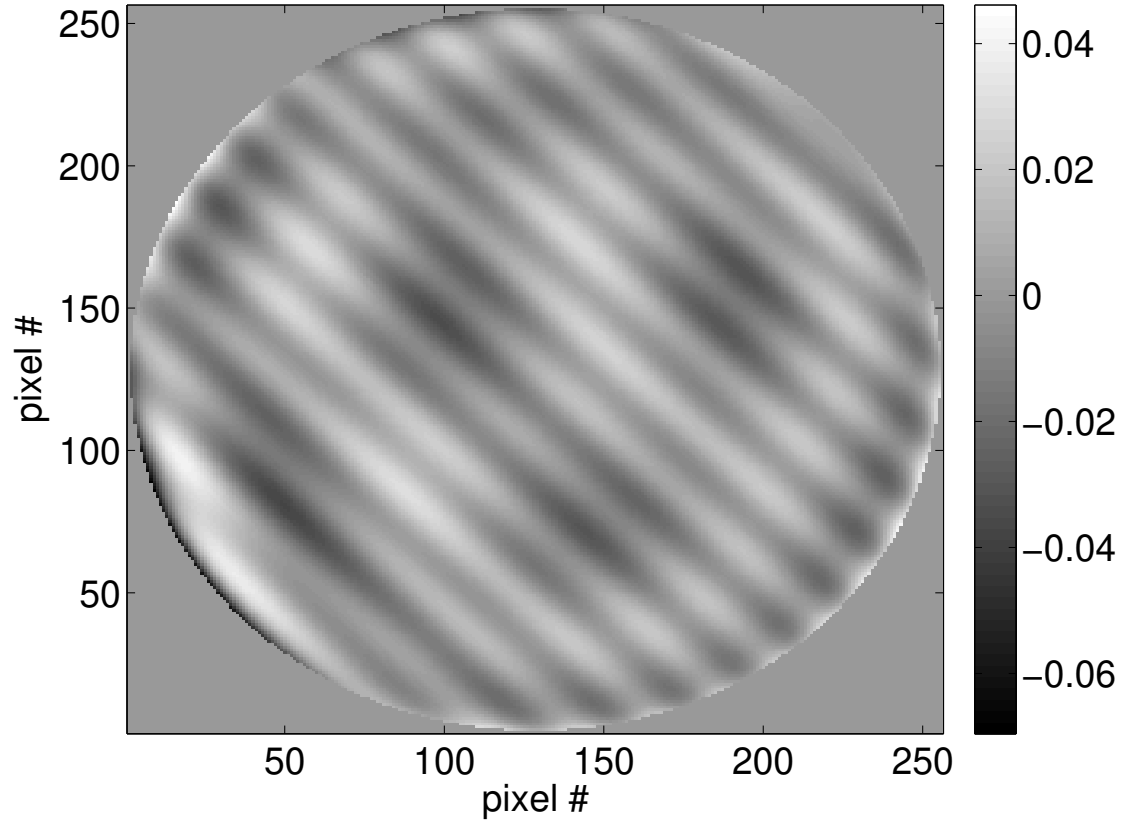


Fig. 5.— The static aberration function assumed for all experiments. This function is composed of a linear combination of high-order Zernike polynomials plus a sinusoid corresponding to the spatial frequency of the planet’s location.

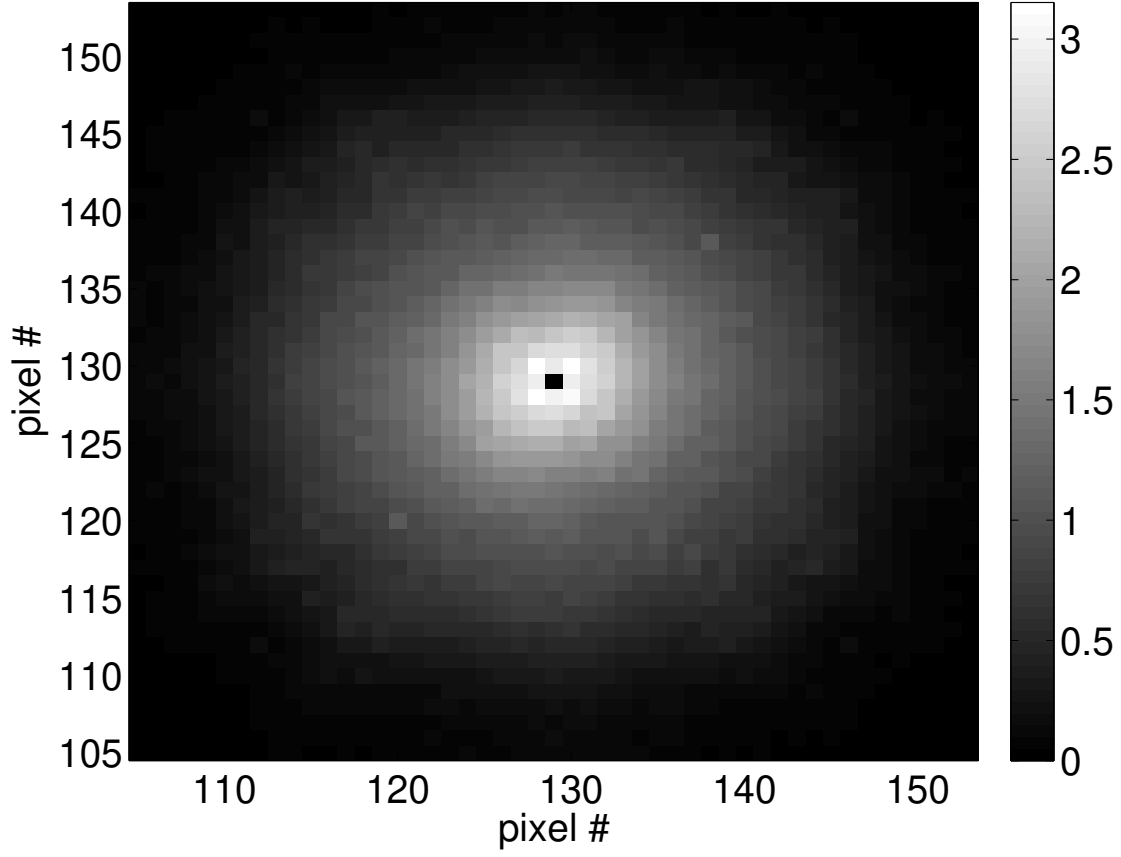


Fig. 6.— The stellar intensity averaged over all 4000 exposures in Experiment 1 without noise. The planet is not included and it is too faint to be seen anyway. The speckle due to the sinusoidal component of the static aberrations can be seen at pixel (120,120), exactly the location of the planet. The colorscale is \log_{10} of the intensity in photons/millisecond/pixel is shown.

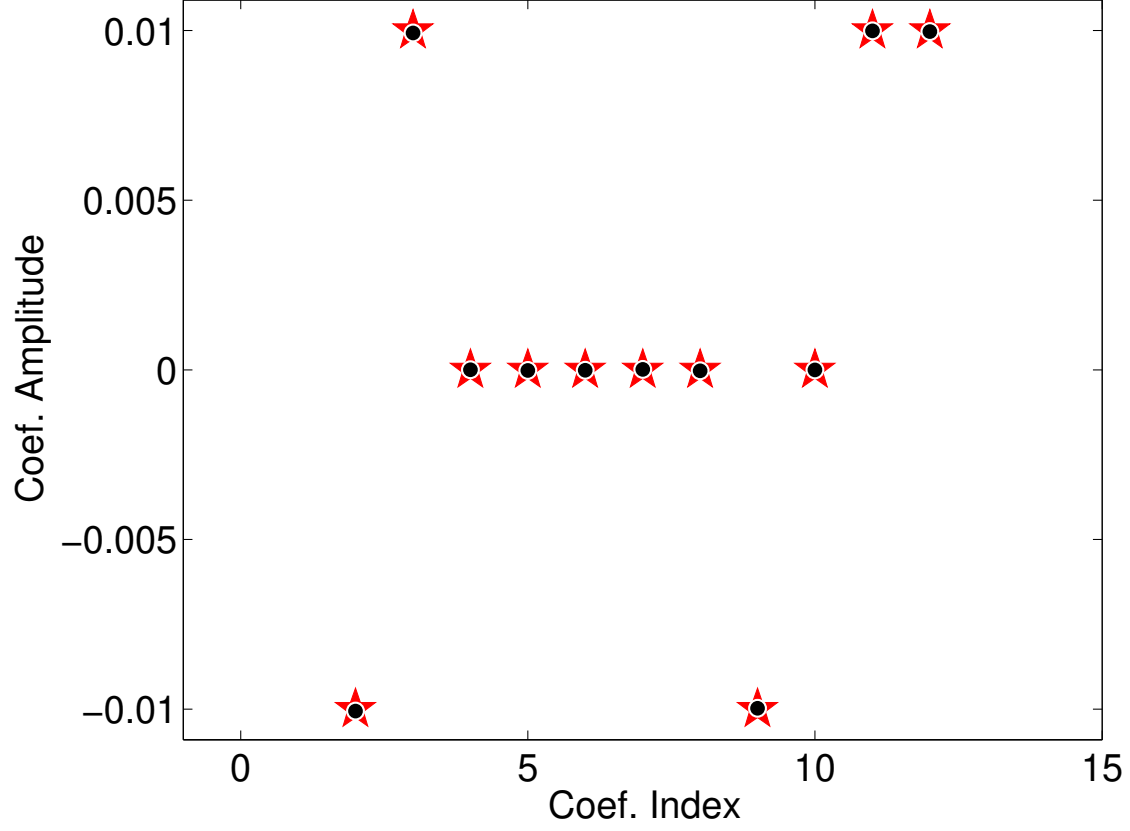


Fig. 7.— (color online) Static aberrations coefficients $\{a_k\}$. The red pentagrams represent the true values used in the simulation, resulting in Fig. 5. The black circles represent the values estimated by the algorithm in Experiment 1, which had 4000 exposures. The error bars, with values of about 3.5×10^{-4} , are smaller than the plotting symbols.

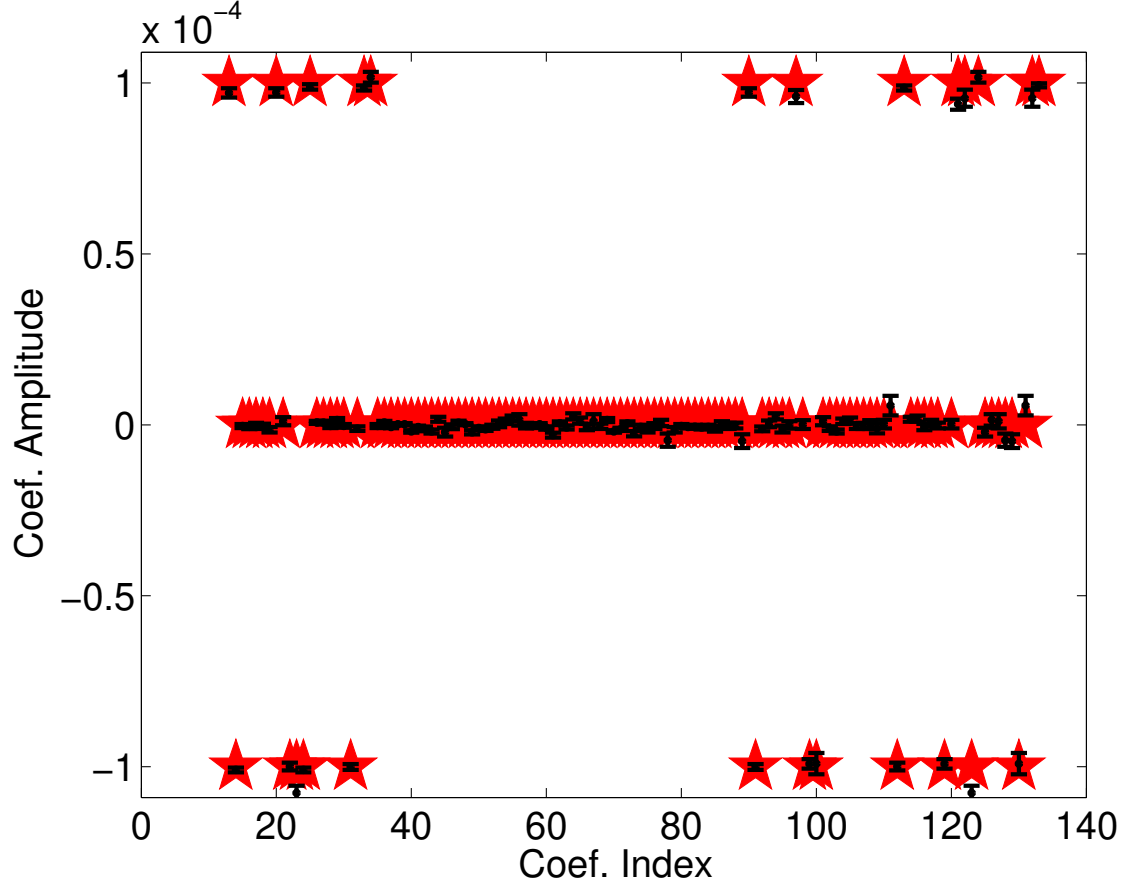


Fig. 8.— (color online) Products of aberrations coefficients $\{a_j a_k\}$. The red pentagrams represent the true values used in the simulation. The black circles represent the values estimated by the algorithm in Experiment 1. The error bars are the square-roots of the diagonal elements of the covariance of the linear estimator.

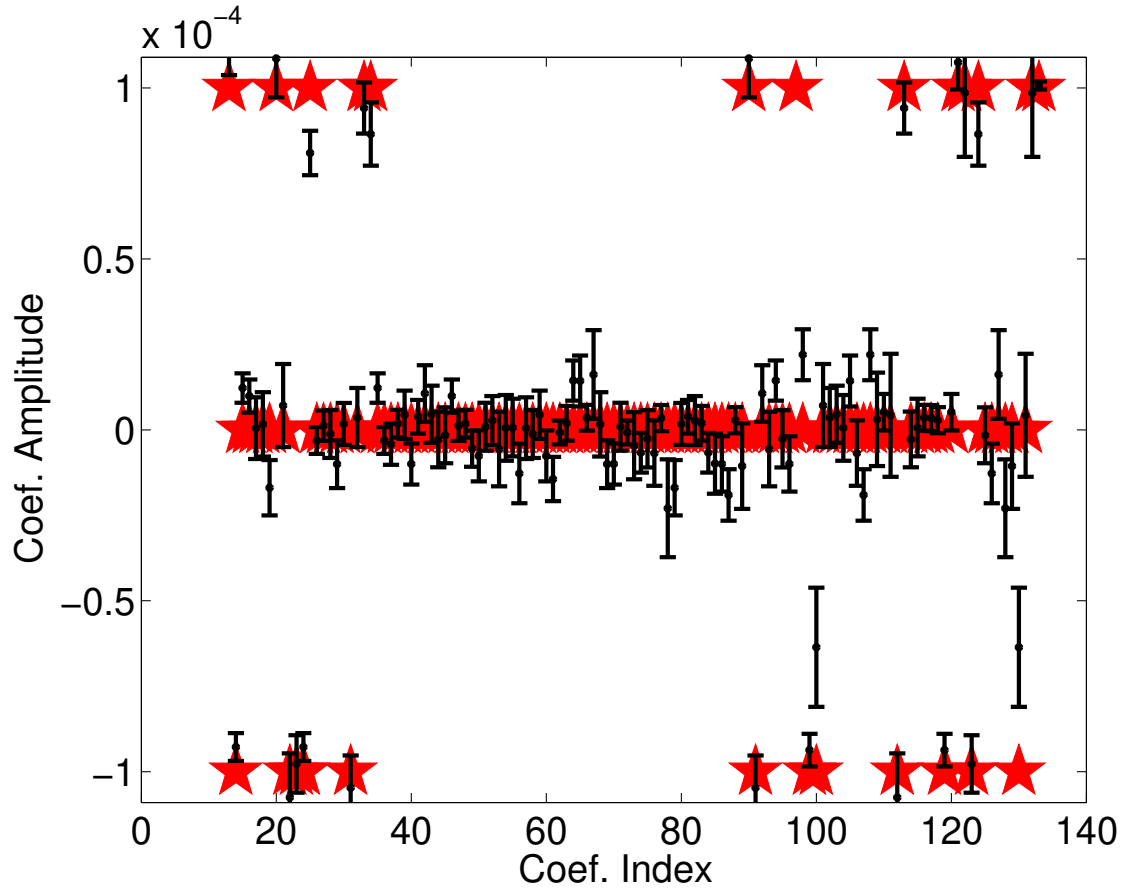


Fig. 9.— (color online) Similar to Fig. 8, except for Experiment 2, which had 1000 exposures.

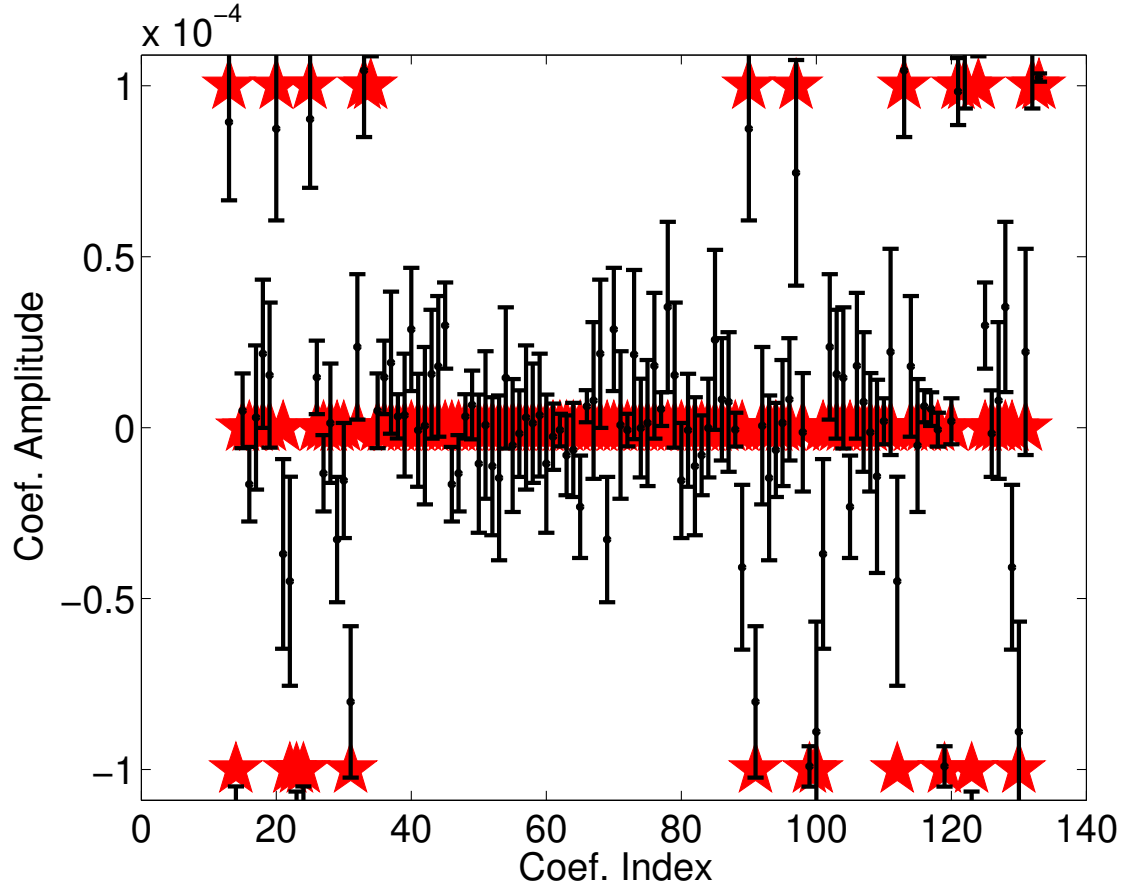


Fig. 10.— (color online) Similar to Fig. 8, except for Experiment 4, which had 1000 exposures and strong planetary emission in a neighboring pixel for which the matrix \mathbf{H} did not account.

references

- Barrett, Harrison H, Dainty, Christopher, Lara, David, “Maximum-likelihood methods in wavefront sensing: stochastic models and likelihood functions,” JOSA A, Vol. 24 Issue 2, pp.391-414 (2007)
- Béchet, Clémentine; Tallon, Michel; Thiébaud, Éric, “Comparison of minimum-norm maximum likelihood and maximum a posteriori wavefront reconstructions for large adaptive optics systems,” JOSA A, Vol. 26 Issue 3, pp.497-508 (2009)
- Bloemhof, E.E., “Anomalous intensity of spinned speckles at high adaptive correction,” Optics Letters, vol. 29, Issue 2, pp. 159-161 (2004)
- Caucci, L., Barrett, H.H., Devaney, N., Rodríguez, J.J., “Application of the Hotelling and ideal observers to detection and localization of exoplanets,” JOSA A, Vol. 24, Issue 12, pp. B13-24 (2007)
- Caucci, L., Barrett, H.H., Rodríguez, J.J., “Spatio-temporal Hotelling observer for signal detection from image sequences,” Optics Express, Vol. 17, Issue 13, pp. 10946-10958 (2009)
- Fusco, T., Conan, J.-M., “On- and off-axis statistical behavior of adaptive-optics-corrected short-exposure Strehl ratio,” JOSA A, Vol. 21, Issue 7, pp. 1277-1289 (2004)
- Gladysz, S., Yaitskova, N., Christou, J.C., “Statistics of intensity in adaptive-optics images and their usefulness for detection and photometry of exoplanets,” JOSA A, Vol. 27, Issue 11, pp.64-75 (2010)
- Labeyrie, A., “Images of exo-planets obtainable from dark speckles in adaptive optics,” Astronomy & Astrophysics, Vol. 298, pp. 544-548 (1995)
- Lafrenière, D., Marois, C., Doyon, R., Nadeau, D., Artigau, É., “A New Algorithm for Point-Spread Function Subtraction in High-Contrast Imaging: A Demonstration with Angular Differential Imaging,” ApJ, 660, 770 (2007)
- Lyot, B., “The study of the solar corona and prominences without eclipses,” MNRAS, Vol. 99, pp. 580-594 (1939)
- Marois, C., Lafrenière, D., Doyon, R., Macintosh, B., Nadeau, D., “Angular Differential Imaging: A Powerful High-Contrast Imaging Technique,” ApJ, 641, 556 (2006)
- Roberts, L.C., Jr., Neyman, C., “Characterization of the AEOS Adaptive Optics System,” PASP, vol. 114, pp.1260-1266 (2002)
- Roggemann, M.C. and Meinhardt, J.A., “Image Reconstruction by means of wave-front

sensor measurements in closed-loop adaptive-optics systems,” JOSA A vol. 10, pp. 1996-2007 (1993)

Sauvage, J.-F., Mugnier, L.M., Rousset, G., Fusco, T., “Analytical expression of long-exposure adaptive-optics-corrected coronagraphic image. First application to exoplanet detection,” JOSA A, Vol. 27, Issue 11, pp. 157-170 (2010)

Soummer, R., Pueyo, L., Larkin, J., “Detection and Characterization of Exoplanets and Disks using Projections on Karhunen-Lo‘eve Eigenimages,” ApJL, *In Press* (2012)

Van Huffel, Sabine, and Vanderwalle, Joos, eds., “The Total Least Squares Problem: Computational Aspects and Analysis” (SIAM, Philadelphia, 1991).